

A Structural and Magnetic Investigation of the Inversion Degree in Ferrite Nanocrystals MFe_2O_4 (M = Mn, Co, Ni)

D. Carta,[†] M. F. Casula,[†] A. Falqui,[†] D. Loche,[†] G. Mountjoy,^{†,‡} C. Sangregorio,[§] and A. Corrias^{*,†}

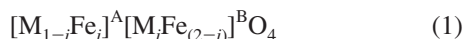
Dipartimento di Scienze Chimiche and INSTM, Università di Cagliari, S.P. Monserrato-Sestu, Km 0.700, I-09042 Monserrato, Cagliari, Italy, and Dipartimento di Chimica and INSTM, Università di Firenze, Via della Lastruccia 3, I- 50019 Sesto Fiorentino, Italy

Received: February 5, 2009; Revised Manuscript Received: March 27, 2009

The structural and magnetic properties of nanocrystalline manganese, cobalt, and nickel spinel ferrites dispersed in a highly porous SiO_2 aerogel matrix were studied. X-ray diffraction and high-resolution transmission electron microscopy indicate that single crystalline ferrite nanoparticles are well dispersed in the amorphous matrix. The cation distribution between the octahedral and tetrahedral sites of the spinel structure was investigated by X-ray absorption spectroscopy. The analysis of both the X-ray absorption near edge structure and the extended X-ray absorption fine structure indicates that the degree of inversion of the spinel structure increases in the series Mn, Co, and Ni spinel, in accordance with the values commonly found in the corresponding bulk spinels. In particular, fitting of the EXAFS data indicates that the degree of inversion in nanosized ferrites is 0.20 for MnFe_2O_4 , 0.68 for CoFe_2O_4 , and 1.00 for NiFe_2O_4 . Magnetic characterization further supports these findings.

1. Introduction

Spinel ferrites are a class of compounds of general formula MFe_2O_4 (M = Mn, Co, Ni, Zn, Mg, etc.), which are of great interest for their remarkable magnetic, catalytic, optical, and electrical properties. The spinel structure belongs to space group $Fd3m$. The cubic unit cell is formed by 56 atoms, 32 oxygen anions distributed in a cubic close packed structure, and 24 cations occupying 8 of the 64 available tetrahedral sites (A sites) and 16 of the 32 available octahedral sites (B sites).¹ The structural formula for a generic spinel compound MFe_2O_4 can be written as²



where the amounts in brackets represent the average occupancy of A sites and B sites and i is the *inversion parameter*. Depending on cation distribution, a spinel can be *normal*, *inverse*, or *partially inverse*. In a *normal* spinel structure, the 8 bivalent cations are all located in tetrahedral sites and the 16 trivalent cations are all located in octahedral sites, while, in an *inverse* spinel structure, the 8 bivalent cations occupy 8 octahedral sites and the 16 trivalent cations are distributed between 8 tetrahedral and 8 octahedral sites.³ For a normal spinel, $i = 0$, and for an inverted spinel, $i = 1$. If the bivalent cations are present on both tetrahedral and octahedral sites, the spinel is *partially inverted* and $0 < i < 1$.

Since the peculiar properties of ferrites are strictly related to the distribution of cations between octahedral and tetrahedral sites in the spinel structure, the control of cation distribution provides a means to tailor their properties. Therefore, there is

a particular interest in studying the cation distribution in ferrites. Cation distribution depends on the electronic configuration and valence of ions. Some studies show that particle size can also be influential, in particular at the nanometric scale.

Nanoparticles of transition metal spinel ferrites have been the subject of increasing interest due to their magnetic and catalytic properties, different from those of bulk materials.⁴ Transition metal ferrite nanoparticles find applications in magnetic storage systems,⁵ site-specific drug delivery,⁶ magnetic resonance imaging,⁷ and photomagnetic materials.⁸ The peculiarity in the properties of ferrite nanoparticles depends on both size and cation distribution. With decreasing particle size, the surface area increases, improving the catalytic properties. Moreover, each nanoparticle can be considered as a single magnetic domain. Some authors suggested that changes in the particle size can influence magnetic properties due to change in cation distribution.⁹

Spinel ferrite nanoparticles can be prepared by a variety of methods such as hydrothermal synthesis,¹⁰ ball-milling,¹¹ coprecipitation,¹² combustion reaction,¹³ and the reverse micelles technique.¹⁴ However, nonsupported ferrite nanoparticles have the tendency to aggregate, with negative effects on both magnetic and catalytic properties. The dispersion of the nanoparticles in an amorphous matrix provides a solution to this problem, giving rise to magnetic nanocomposite materials where the nanoparticles are homogeneously dispersed in the matrix. Nanocomposites of ferrite nanoparticles can be prepared using the melt quenching route. However, the high temperatures required by this method often lead to the reduction of Fe^{3+} to Fe^{2+} .¹⁵ Therefore, the low-temperature sol–gel synthetic route appears to be more suitable for the synthesis of these systems. Moreover, excellent control of composition, purity, homogeneity, particle sizes, and distribution can be obtained. Nanocomposites of ferrite nanoparticles dispersed in a silica matrix have been successfully synthesized using the sol–gel route.^{16–18} In this work, nanocomposites containing MnFe_2O_4 , CoFe_2O_4 , and

* To whom correspondence should be addressed. E-mail: corrias@unica.it. Fax: +39 0706754388.

[†] Università di Cagliari.

[‡] Permanent address: School of Physical Sciences, Ingram Building, University of Kent, Canterbury, CT2 7NH, U.K.

[§] Università di Firenze.

NiFe₂O₄ nanoparticles dispersed in a highly porous aerogel silica host are studied.

Bulk MnFe₂O₄, CoFe₂O₄, and NiFe₂O₄ all have a spinel structure, but they differ in the distribution of the cations among the octahedral and tetrahedral sites in the structure. MnFe₂O₄ is a *partially inverted* spinel structure with manganese ions predominantly in the tetrahedral sites (low degree of inversion).¹⁹ Typically, MnFe₂O₄ has a degree of inversion of $i = 0.20$ corresponding to 20% Mn²⁺ in octahedral sites.^{20,21} CoFe₂O₄ is a *partially inverted* spinel structure with cobalt atoms predominantly in the octahedral sites (high degree of inversion).²² An inversion parameter of $i = 0.80$ has been reported in a dated work,²³ indicating a structure with 80% Co²⁺ in octahedral sites. Lower degrees of inversions ranging between 0.68 and 0.74 were also reported.^{24–26} NiFe₂O₄ is a *totally inverted* spinel structure with all nickel ions in the octahedral sites ($i = 1$).²⁷

Extended X-ray absorption fine structure (EXAFS) and X-ray absorption near edge structure (XANES) have been shown to be powerful tools for the structural study of metal oxide, alloys and ferrite nanoparticles and nanocomposites prepared by the sol–gel process.^{28–32} These techniques are element-specific and sensitive to the local structure,³³ making them ideal for studying multicomponent dilute and disordered materials. EXAFS gives information about bond distances and coordination numbers of shells surrounding the absorbing atom; XANES gives information on the site symmetry and oxidation state of the absorbing atom. Moreover, EXAFS has been recently found to be a useful tool to determine the cation distribution in ferrite spinels.^{26,34,35} In particular, the combined use of XANES and EXAFS at both the Fe³⁺ and M²⁺ edges seems to have superior capabilities with respect to other probes used to the same end, such as X-ray (XRD) and neutron (ND) diffraction³⁶ and Mössbauer spectroscopy.²⁰ In fact, XRD cannot distinguish Fe from Mn/Co/Ni due to their similar scattering factors. Mössbauer spectroscopy is effective in determining the environment of Fe³⁺ ions but does not provide information on the M²⁺ cations and is not very effective for dilute samples.³⁷

In this paper, a detailed structural and magnetic characterization of nanoparticles of Mn, Co, and Ni ferrites dispersed in a highly porous silica aerogel matrix, with a composition of 10 wt % MFe₂O₄/(MFe₂O₄ + SiO₂), M = Mn, Co, Ni, is carried out with the main aim of investigating the degree of inversion of these ferrites in the nanometer range. XRD and high-resolution transmission electron microscopy are used to gather information on the phases present and on their dimension. EXAFS and XANES are used to determine quantitatively the degree of inversion of the nanoparticles of Mn, Co, and Ni ferrites. Magnetic characterization is also carried out to complement the study.

2. Experimental Section

The samples were prepared by the sol–gel process using tetraethoxysilane ((Si(OC₂H₅)₄, Aldrich, 98%, TEOS) as a precursor for silica, iron(III) and manganese(II), cobalt(II) or nickel(II) nitrates (Fe(NO₃)₃·9H₂O, Aldrich, 98%, Mn(NO₃)₂·6H₂O, Aldrich, 98%, Co(NO₃)₂·6H₂O, Aldrich, 98%, and Ni(NO₃)₂·6H₂O, Aldrich, 100%) as precursors for the ferrite phases, and absolute ethanol (EtOH, Fluka) as a mutual solvent. The precursors were added in such a way to obtain nanocomposites containing a nominal ratio of 10 wt % MFe₂O₄/(MFe₂O₄ + SiO₂), where M = Mn, Co, or Ni. The ethanolic solution of the metal salts was added into the prehydrolyzed TEOS under acidic catalysis. A hydroalcoholic solution of urea (NH₂CONH₂, Aldrich, >99.0%) was then added under reflux for 2 h at 85 °C

as a basic gelation agent. The sols were left in a closed container at 40 °C; gelation occurred after less than 1 day for the samples containing Mn and Ni and after less than 2 days for the sample containing cobalt. The alcogels were submitted to high-temperature supercritical drying in an autoclave (Parr, 300 cm³). The gel is inserted in the autoclave filled with an appropriate amount of ethanol and flushed with N₂ before being heated in such a way to take the solvent to the supercritical state (i.e., 330 °C, 70 atm). The autoclave was then vented, and highly porous aerogel samples were obtained. The samples containing Co and Ni were thermally treated at 900 °C for 1 h in air, while the sample containing Mn was thermally treated at 900 °C for 1 h in argon to avoid oxidation of Mn²⁺ to Mn³⁺. The samples will be hereafter called AFeM, where M refers to the bivalent cation (Mn, Co, Ni). More details about the synthesis can be found in refs 26, 34, and 35.

XRD spectra were recorded on a X3000 Seifert diffractometer equipped with a graphite monochromator on the diffracted beam. The scans were collected within the range 10–80° (2 θ) using Cu K α radiation. The average size of crystallite domains was calculated using the Scherrer formula, determining instrumental broadening using a standard Si sample.³⁸

High-resolution transmission electron microscopy (HREM) analysis was carried out by means of a Jeol JEM-2100F microscope (samples AFeNi and AFeMn) and of a FEI Tecnai F20 microscope (sample AFeCo), both equipped with a field emission electron source and operating at 200 kV. The FEI microscope was also equipped with a corrector of objective lens spherical aberration.

EXAFS and XANES spectra of samples AFeCo and AFeNi were recorded at beamline 11.1 (XAFS) of the ELETTRA synchrotron (Trieste, Italy), while EXAFS and XANES spectra of AFeMn were recorded at station 7.1 of the SRS, Daresbury Laboratory, U.K.

Spectra at the Fe (7112 eV), Mn (6539 eV), Co (7709 eV), and Ni (8333 eV) K-edges were acquired at room temperature in transmission mode using a Si(111) monochromator. Data were also collected on reference compounds. Samples with a suitable and highly uniform optical thickness were prepared from powders by pressing them into a cardboard frame with mylar windows without the need of using any diluent, the aerogels being very easy to compress due to their very low apparent density.

The program Viper was used to sum the data, identify the beginning of the absorption edge, E_0 , fit pre- and post-edge backgrounds, and hence obtain the normalized absorbance χ as a function of the modulus of the photoelectron wavevector k .³⁹ The modular package DL_EXCURV,⁴⁰ based on the EXCURV98 code, was used in the final stage of data processing to model the experimental $\chi(k)$ in order to extract structural information. This code uses fast curved wave theory⁴¹ and calculates *ab initio* the effective curved wave backscattering amplitude of the scatterer, the phase shift due to the absorbing atom potential, the phase shift due to the scatterer, and the inelastic mean free path of the photoelectron.^{42,43} The S_0 parameter (called AFAC in EXCURV98), which is the many-body amplitude reduction factor, was determined to be 0.9 from fitting to the reference samples. The parameter EF, which is a correction to E_0 , was free to vary in all fittings. The structural parameters were obtained by nonlinear least-squares fitting in k space with a k^3 weighting to emphasize the high-energy part of the spectrum. The fitting was carried out using the k range 2.5–12 Å^{−1}, at all edges. Note that, since the Fe K-edge follows the Mn K-edge and the Co K-edge follows the Fe K-edge, the

available k range for Mn in manganese ferrite and for Fe in cobalt ferrite is limited to a maximum value of $k = 12 \text{ \AA}^{-1}$. The errors in the fit parameters were obtained from the 95% confidence level, as calculated in EXCURV98. The number of fitted parameters was always less than the number of statistically independent data points, as estimated in the standard way.⁴⁴ The quality of the fit was judged from the normalized sum of residuals

$$R\text{-factor} = \frac{\sum_n k_n^3 |\chi_{\text{expt}}(k_n) - \chi_{\text{fit}}(k_n)|}{\sum_n k_n^3 |\chi_{\text{expt}}(k_n)|} \times 100 \quad (2)$$

R -factors were calculated both on the experimental $k^3\chi(k)$ and on the data obtained by backtransforming the Fourier transforms (FTs) in the R space corresponding to the shells which were fitted. The second value, named the *R -factor, is more meaningful in stating the goodness of the fit, since the backtransforms do not contain low R contributions due to imperfect background removal and high R contributions which were not introduced in the fit. Reasonable EXAFS fits of single shells typically have R -factor values around 20%; however, when the fit is performed on the total EXAFS spectra, higher values of R -factor can still correspond to good fits especially if the fit is not extended to peaks at high R .

The XANES spectra were processed in the usual way to obtain normalized absorbance.⁴⁵ XANES at the K-edge involves the excitation of a 1s photoelectron into low-lying empty states at the central atom with p-type symmetry. The characteristic features of the XANES spectra for transition metal oxides⁴⁶ are as follows. An increase in valence of the metal atom causes a shift to higher energies. Pre-edge peak(s) may occur at about 15–20 eV before the main K-edge corresponding to 1s to 3d transitions with 3d–4p mixing. The pre-edge peak increases in intensity as the degree of centrosymmetry of the metal atom environment decreases. The main peak and shoulders of the absorption edge corresponds to transitions to 4p continuum states and “shape resonances” of the metal atom environment. For a given environment, the main peak is broadened by disorder in the nearest neighbor distances. Secondary peaks occurring a few 10 eV above the main peak correspond to multiple scattering from neighboring atom shells.

The pre-edge peak has well-known behavior for sites with tetrahedral and octahedral symmetry (i.e., those present in spinels), being narrower and more intense for the former and broader and less intense for the latter. This is primarily because tetrahedral symmetry is highly noncentrosymmetric and this enables $p \rightarrow d$ transitions which contribute to the pre-edge peak.⁴⁷ In addition, the shape of the pre-edge peak is influenced by the splitting of d-states which is different for tetrahedral and octahedral site symmetry.^{47,48} The typical splitting is 1.5 eV, but the core-hole lifetime at the Fe K-edge is 1.15 eV,⁴⁷ so the splitting cannot be observed with the monochromator used in the present study which had an energy resolution of 1.0 eV. When both tetrahedral and octahedral sites are occupied, the pre-edge peak will be the sum of these contributions, and will increase in intensity directly with the proportion of tetrahedral sites.^{47,49} The pre-edge peak position increases slightly by ~ 0.3 eV in going from tetrahedral to octahedral site symmetry^{49,50} (which is small compared to the ~ 1.5 eV increase in pre-edge peak position when oxidation increases from +2 to +3).^{47,50} This behavior is well documented for Fe^{47,48,50} and Ni,⁴⁹ and has also been seen for Mn.⁵¹ There are limited reports on XANES of Co reference oxides,⁵² but the same behavior is expected.

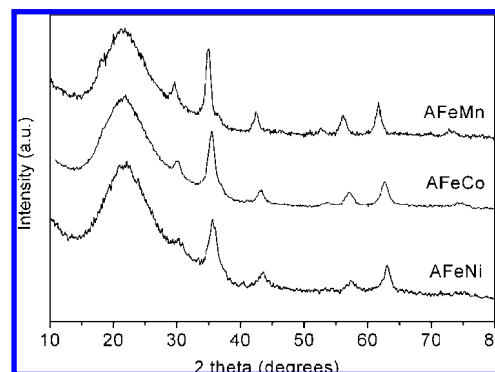


Figure 1. XRD patterns of AFeMn, AFeCo, and AFeNi.

Measurements of static magnetization and low-temperature hysteretic behavior were performed on the AFeNi, AFeMn, and AFeCo samples on a Quantum Design MPMS SQUID magnetometer, equipped with a superconducting magnet producing fields up to 50 kOe.

3. Results and Discussion

XRD. The XRD patterns for the AFeMn, AFeCo, and AFeNi samples, reported in Figure 1, show an amorphous halo due to the silica matrix and superimposed peaks due to the corresponding spinel ferrite phases.^{53–55} The position of the peaks shifts slightly to higher scattering angles in the series AFeMn, AFeCo, AFeNi in accordance with the slight decrease of the lattice parameter reported in the literature in the sequence MnFe_2O_4 ($a = 8.499 \text{ \AA}$), CoFe_2O_4 ($a = 8.391 \text{ \AA}$), NiFe_2O_4 ($a = 8.339 \text{ \AA}$).^{53–55} The intensity ratios of the peaks are the same in the three samples. This is not surprising, since XRD is not able to discern between different degrees of inversion of these spinels, the scattering factors of Fe^{3+} on one side and of M^{2+} on the other side being so similar that the XRD pattern does not change significantly when the population of octahedral and tetrahedral sites varies.

The ferrite peaks are quite broad as a consequence of the nanometer size of the crystallite domains. From the full width at half-maximum of the peaks, an average size of 6 nm for AFeNi and AFeCo and of 9 nm for AFeMn was estimated.

HREM. Figure 2 shows the HREM images of a nanoparticle of AFeMn sample (a), AFeCo sample (b), and AFeNi sample (c). The 2D-fast Fourier transform (2D-FFT), corresponding to the squared area indicated in each HREM image, is also reported. The AFeMn, AFeCo, and AFeNi analyzed particles are respectively oriented in the [211], [001], and [323] zone axes. The 2D-FFTs clearly indicate that these particles are single crystals, with lattice parameters corresponding to those expected for the corresponding bulk ferrite.

XANES. Analysis of the XANES region gives information on the oxidation state of the absorbing atom and on its local atomic environment, in particular on the site symmetry. For Mn, Fe, Co, and Ni, the oxidation state can be determined accurately from the position of the main absorption edge in comparison to reference oxides (MnO , Mn_3O_4 , Mn_2O_3 , and MnO_2 for Mn; FeO , Fe_3O_4 , and α - and γ - Fe_2O_3 for Fe; Co_3O_4 and CoO for Co; and NiO for Ni; see the Supporting Information). Typically, the edge position increases by ~ 3 eV when oxidation increases from +2 to +3,^{50,51} and the edge position of a sample can be determined with an accuracy of 0.5 eV.

The XANES spectra for the AFeMn, AFeCo, and AFeNi samples are shown in Figure 3, while the XANES spectra of reference oxides are reported in the Supporting Information.

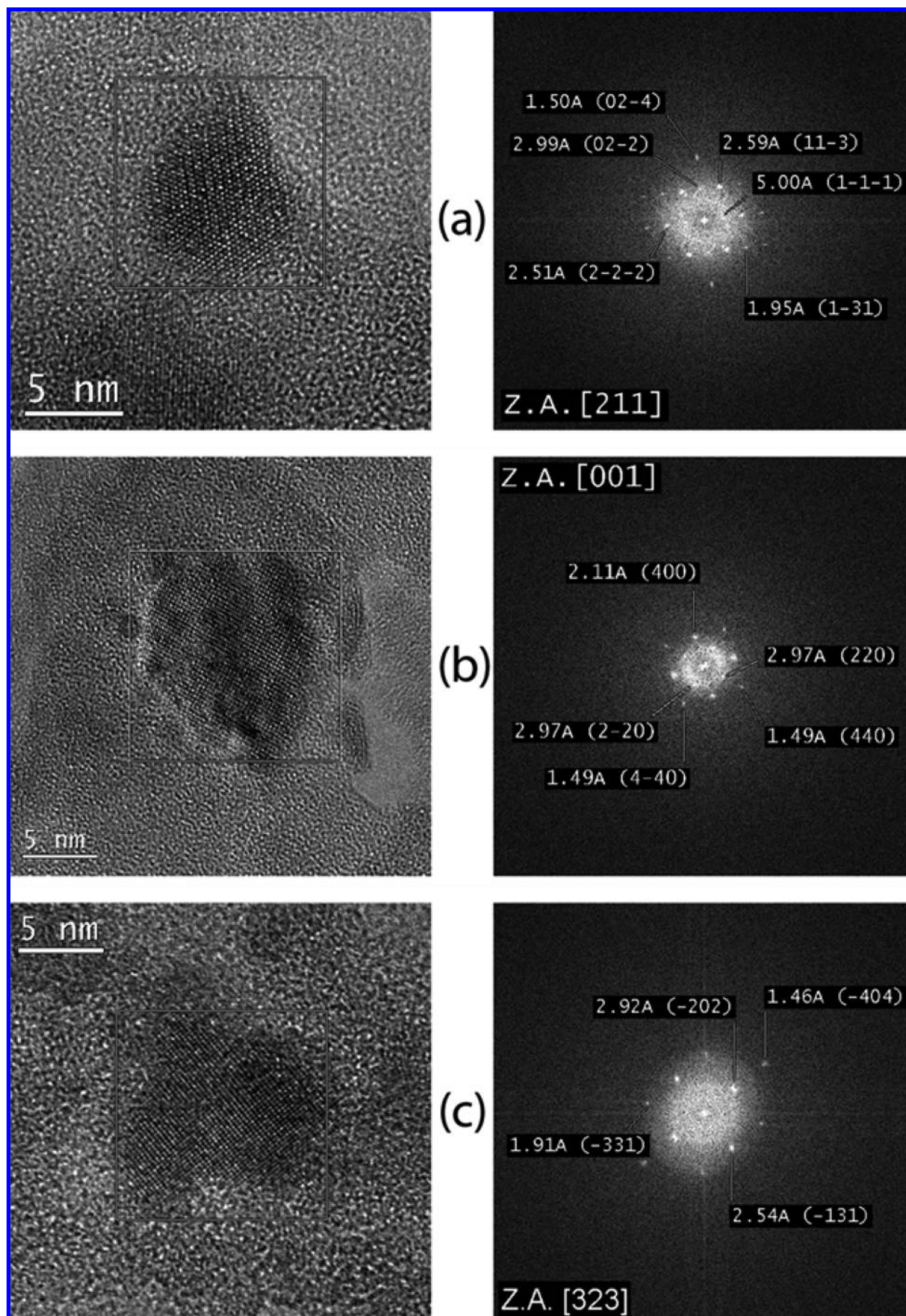


Figure 2. HREM images of a nanoparticle of AFeMn (a), AFeCo (b), and AFeNi (c). The 2D-fast Fourier transform, corresponding to the squared area indicated in each HREM image, is also reported.

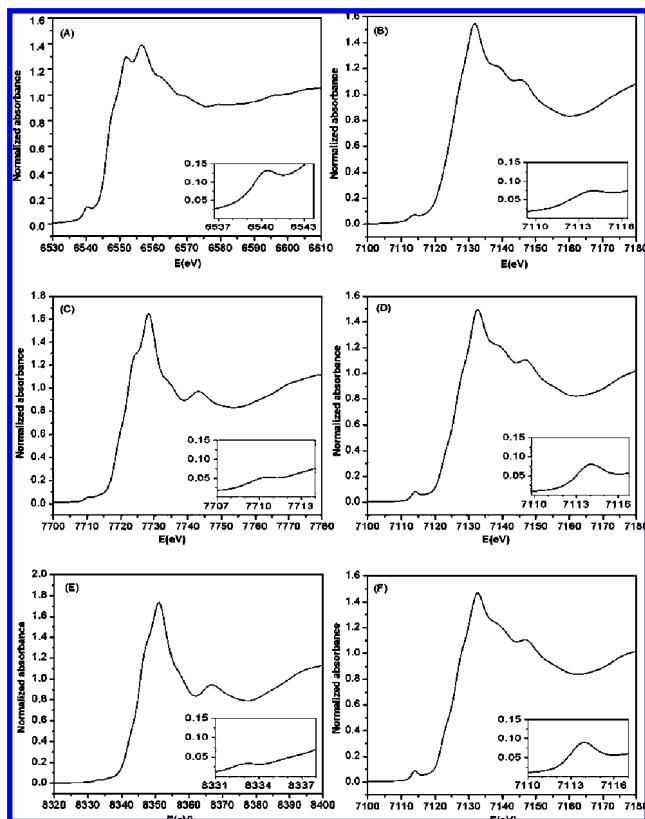


Figure 3. XANES spectra at the Mn (A), Co (C), or Ni (E) K-edge and Fe K-edge for AFeMn (B), AFeCo (D), and AFeNi (F). Inset: Detail of the pre-edge peak.

At the Fe edge, the position of the edge for the AFeMn, AFeCo, and AFeNi samples is typical of Fe^{3+} , and at the other metal (M) edge, the position is typical of Mn, Co, and Ni in the oxidation state +2, as inferred by comparison with the XANES spectra of different M reference oxides.

At the M edge, the pre-edge peak is larger in AFeMn in comparison with the other two samples. In particular, the low intensity of the M^{2+} pre-edge peak in the AFeCo and AFeNi samples indicates that M^{2+} is mostly located in highly centrosymmetric octahedral sites, i.e., high degree of inversion, while in the AFeMn sample the fraction of M^{2+} in highly centrosymmetric octahedral sites is lower, i.e., lower degree of inversion. Moreover, the fraction of M^{2+} in octahedral sites is higher in AFeNi than in AFeCo because the M^{2+} pre-edge peak has lower intensity. The opposite trend is observed at the Fe edge; i.e., the pre-edge peak is larger in AFeNi followed by AFeCo and then by AFeMn.

EXAFS. The EXAFS $k\chi^3(k)$ and corresponding FTs for the AFeMn, AFeCo, and AFeNi samples are reported in Figures 4 and 5, respectively. The $k\chi^3(k)$ values of the three samples show significant differences at both the Fe and M edge, indicating that the structural environment around Fe^{3+} and M^{2+} is different in the three samples. The comparison of the FTs of the three samples is especially informative. In particular, the region between 2.5 and 4 Å, where the most important contributions are the M–M distances, provides qualitative but very helpful information on the degree of inversion of the spinel structure. In these ferrite spinels, the M_B – M_B distances between two octahedral sites are approximately 3 Å, while the M_A – M_B and M_A – M_A distances involving tetrahedral sites are about 3.5 Å. Taking into account that in a normal spinel the M^{2+} ions are all located in tetrahedral sites and in an inverse spinel the M^{2+}

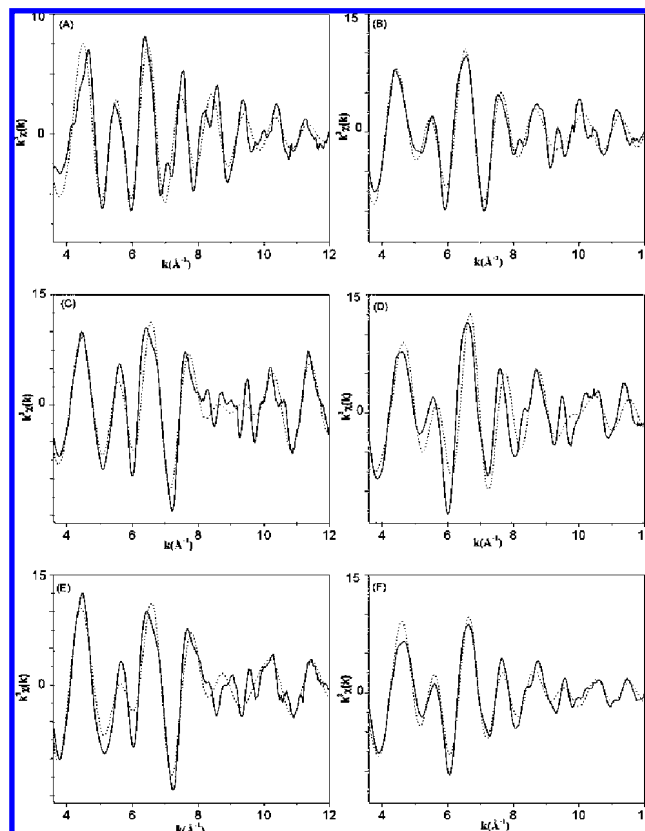


Figure 4. $k^3\chi(k)$ spectra at the Mn (A), Co (C), or Ni (E) K-edge and Fe K-edge for AFeMn (B), AFeCo (D), and AFeNi (F). Experiment (—), fit results (···).

ions are all located in octahedral sites, the contribution around 3 Å in the FT at the M^{2+} K-edge should decrease going from an inverse to a normal spinel, for which the contribution should be zero. The opposite trend should be observed for the contribution around 3.5 Å which should decrease going from a normal to an inverse spinel. Variations in the degree of inversion should also affect the same region of the FT at the Fe K-edge. However, in this case, the effect is less pronounced because in both normal and inverse spinel Fe^{3+} ions occupy octahedral sites, the proportion varying from 100% in normal spinels to 50% in inverse spinels. Taking into account these points, the comparison of the FTs at the Mn, Co, and Ni edge indicates quite clearly that the degree of inversion increases in the series AFeMn, AFeCo, AFeNi.

In order to obtain quantitative information on the degree of inversion, the fitting of the EXAFS data was performed by introducing the typical distances of the spinel ferrites up to about 4 Å in two clusters of atoms, one having the absorbing atom (Fe or Mn/Co/Ni) in tetrahedral sites (hereafter called Fe_A and Mn_A , Co_A , Ni_A) and the other having the absorbing atom (Fe or Mn/Co/Ni) in octahedral sites (hereafter called Fe_B and Mn_B , Co_B , Ni_B). As Fe and Mn/Co/Ni have similar backscattering amplitudes, only Fe backscatters are considered at the Fe edge and only Mn/Co/Ni backscatters are considered at the Mn/Co/Ni edge, in order to simplify the fitting. The distribution of bivalent (Mn, Co, or Ni) and trivalent cations (Fe) between tetrahedral (A) and octahedral (B) sites can be specified by a single variable parameter, $x_\text{B}(\text{M}^{2+})$, i.e., the fraction of M^{2+} cations in octahedral sites, which also corresponds to the inversion parameter, i . The occupancy of tetrahedral (A) sites is determined from $x_\text{A} = 1 - x_\text{B}$. The fraction of Fe^{3+} in octahedral sites must satisfy the requirement $x_\text{B}(\text{Fe}^{3+}) = (2 -$

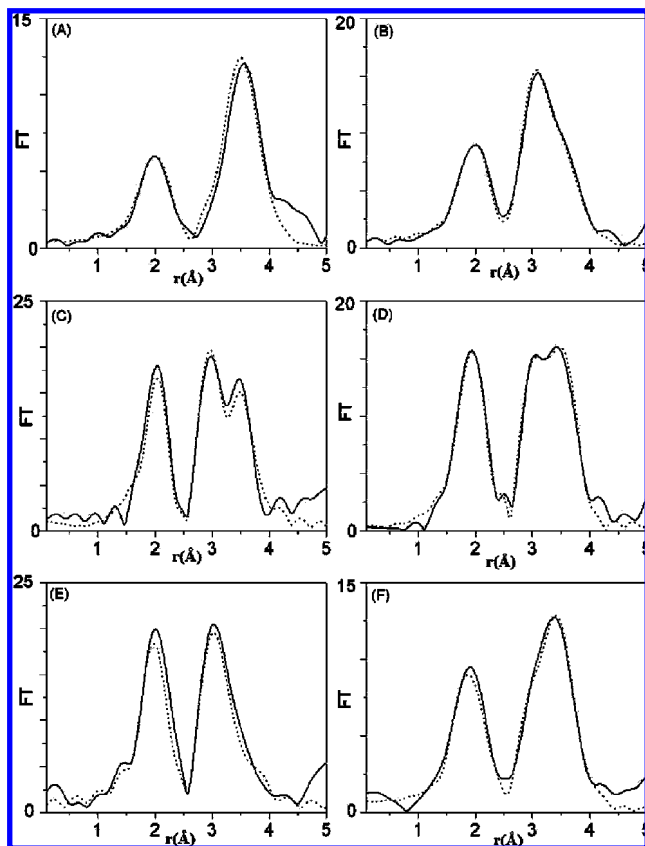


Figure 5. Fourier transforms at the Mn (A), Co (C), or Ni (E) K-edge and Fe K-edge for AFeMn (B), AFeCo (D), and AFeNi (F). Experiment (—), fit results (···).

$x_B(\text{M}^{2+})/2$. In addition to x_B , the other parameters left free to vary were R_i , $2\sigma_i^2$, and EF.

Coordination numbers in the two clusters, N_i , were kept fixed. As it is well-known, in nanocrystalline materials, EXAFS oscillations are smaller than in the corresponding bulk materials due either to a reduction of the coordination number of the outer shells or to an increase of the Debye–Waller factors. In fact, in nanocrystalline materials, a reduction of coordination numbers of outer shells is expected due to the large fraction of atoms in sites near the surface, i.e., with incomplete coordination spheres. The increase in Debye–Waller factors is also expected due to the higher disorder of the surface sites. Since coordination numbers and Debye–Waller factors are strongly correlated, it is not easy to separate the two contributions when fitting the EXAFS data. However, while an increase in Debye–Waller factors always occurs in nanocrystalline materials, the effect being more and more evident as the particle size decreases, the reduction of coordination numbers of outer shells only begins to be detectable when the particles are smaller than 5 nm.⁵⁶ Therefore, since the average size of the nanoparticles of the AFeMn, AFeCo, and AFeNi samples is larger than 6 nm, N_i were kept fixed during the fitting and only the Debye–Waller terms were left free to vary in order to limit the number of free parameters. Best fitting parameters are reported in Tables 1, 2, and 3, respectively.

In all samples at the Fe edge, the first peak near 2 Å is due to two Fe–O bond distances, $\text{Fe}_A\text{–O}$ and $\text{Fe}_B\text{–O}$, corresponding to the tetrahedral sites and the octahedral sites, respectively. The double peak in the region 2.5–4 Å is the overlapping of the contribution from the $\text{Fe}_B\text{–Fe}_B$ and a series of other contributions at higher R values, the most important being

TABLE 1: Interatomic Distances (R), Debye–Waller Factors (σ), and Fraction of Cations in Sites A (x_A) and B (x_B) Obtained by Fitting the Experimental EXAFS Spectra of AFeMn at the Fe and Mn K-Edge^a

Fe K-edge				Mn K-edge			
R (Å)		N	$2\sigma^2$	R (Å)		N	$2\sigma^2$
$x_B = 0.90(3)$				$x_B = 0.20(2)$			
O	2.04(1)	6.0	0.025(2)	O	2.11(4)	6.0	0.030(3)
Fe	3.01(1)	6.0	0.018(1)	Mn	3.00(4)	6.0	0.030(4)
Fe	3.52(1)	6.0	0.021(2)	Mn	3.53(3)	6.0	0.025(5)
O	3.65(1)	2.0	0.021(2)	O	3.66(5)	2.0	0.030(3)
O	3.69(1)	6.0	0.030(1)	O	3.69(8)	6.0	0.040(1)
$x_A = 0.10(3)$				$x_A = 0.80(2)$			
O	1.89(1)	4.0	0.028(1)	O	2.05(1)	4.0	0.030(3)
Fe	3.52(3)	12.0	0.021(8)	Mn	3.53(4)	12.0	0.025(1)
O	3.53(1)	12.0	0.022(3)	O	3.62(2)	12.0	0.040(2)
Fe	3.68(8)	4.0	0.030(2)	Mn	3.67(2)	4.0	0.030(6)
$E_0 = 7127.3$ eV				$E_0 = 8345.6$ eV			
$R\text{-factor} = 31\%$				$R\text{-factor} = 46\%$			
$*R\text{-factor} = 16\%$				$*R\text{-factor} = 24\%$			

^a Values of E_0 , R -factor, and $*R$ -factor are also reported. Coordination numbers (N) were kept fixed.

TABLE 2: Interatomic Distances (R), Debye–Waller Factors (σ), and Fraction of Cations in Sites A (x_A) and B (x_B) Obtained by Fitting the Experimental EXAFS Spectra of AFeCo at the Fe and Co K-Edge^a

Fe K-edge				Co K-edge			
R (Å)		N	$2\sigma^2$	R (Å)		N	$2\sigma^2$
$x_B = 0.66(2)$				$x_B = 0.68(3)$			
O	1.98(1)	6.0	0.012(1)	O	2.06(1)	6.0	0.010(1)
Fe	2.98(1)	6.0	0.018(1)	Co	2.95(1)	6.0	0.012(1)
Fe	3.48(1)	6.0	0.019(1)	Co	3.47(1)	6.0	0.018(1)
O	3.56(1)	2.0	0.015(1)	O	3.56(5)	2.0	0.018(1)
O	3.66(2)	6.0	0.015(1)	O	3.66(2)	6.0	0.018(1)
$x_A = 0.34(2)$				$x_A = 0.32(3)$			
O	1.84(1)	4.0	0.017(1)	O	1.89(3)	4.0	0.020(2)
Fe	3.48(1)	12.0	0.019(1)	Co	3.47(1)	12.0	0.018(1)
O	3.50(1)	12.0	0.014(1)	O	3.50(3)	12.0	0.018(1)
Fe	3.54(3)	4.0	0.024(2)	Co	3.54(6)	4.0	0.026(2)
$E_0 = 7127.7$ eV				$E_0 = 7723.4$ eV			
R -factor = 27%				R -factor = 37%			
* R -factor = 15%				* R -factor = 22%			

^a Values of E_0 , R -factor, and $*R$ -factor are also reported. Coordination numbers (N) were kept fixed.

$\text{Fe}_A\text{–Fe}_A$ and $\text{Fe}_A\text{–Fe}_B$. Similar observations can be made for the M^{2+} edge. The first peak arises from the two distances $\text{M}_A\text{–O}$ and $\text{M}_B\text{–O}$ due to tetrahedrally and octahedrally coordinated M, while the first component of the double peak corresponds to the $\text{M}_B\text{–M}_B$ distances and the second component to several contributions, the most important being $\text{M}_A\text{–M}_A$ and $\text{M}_A\text{–M}_B$. It has to be noted that the first shell distance $\text{Mn}_A\text{–O}$ in AFeMn is longer than the $\text{M}_A\text{–O}$ distances in Co and Ni samples. This is consistent with the larger ionic radius of Mn^{2+} compared to Co^{2+} and Ni^{2+} .²¹

As already mentioned, the degree of inversion i was determined by fitting the fraction of tetrahedral (A) and octahedral (B) sites occupied by Fe^{3+} and Co^{2+} , Ni^{2+} , and Mn^{2+} . The results of the fitting confirm that the degree of inversion increases in the series AFeMn ($i = 0.20 \pm 0.02$), AFeCo ($i = 0.68 \pm 0.03$), AFeNi ($i = 1.00 \pm 0.02$).

In AFeMn with $i = 0.20$, 80% of Mn^{2+} occupies tetrahedral sites and 20% of Mn^{2+} occupies octahedral sites while 10% of Fe^{3+} occupies tetrahedral sites and 90% occupies octahedral

TABLE 3: Interatomic Distances (R), Debye–Waller Factors (σ), and Fraction of Cations in Sites A (x_A) and B (x_B) Obtained by Fitting the Experimental EXAFS Spectra of AFeNi at the Fe and Ni K-Edge^a

Fe K-edge				Ni K-edge			
	R (Å)	N	$2\sigma^2$		R (Å)	N	$2\sigma^2$
$x_B = 0.50(3)$				$x_B = 1.00(2)$			
O	2.04(1)	6.0	0.015(1)	O	2.04(1)	6.0	0.014(1)
Fe	2.95(1)	6.0	0.023(1)	Ni	2.94(1)	6.0	0.018(2)
Fe	3.46(1)	6.0	0.021(1)	Ni	3.46(1)	6.0	0.018(2)
O	3.52(5)	2.0	0.036(2)	O	3.52(4)	2.0	0.020(2)
O	3.64(2)	6.0	0.031(1)	O	3.64(2)	6.0	0.018(4)
$x_A = 0.50(3)$							
O	1.89(1)	4.0	0.010(1)				
Fe	3.46(1)	12.0	0.021(5)				
O	3.47(2)	12.0	0.040(2)				
Fe	3.61(3)	4.0	0.021(4)				
$E_0 = 7127.3$ eV				$E_0 = 8345.6$ eV			
R -factor = 33%				R -factor = 34%			
$*R$ -factor = 25%				$*R$ -factor = 25%			

^a Values of E_0 , R -factor, and $*R$ -factor are also reported. Coordination numbers (N) were kept fixed.

sites. The degree of inversion is the same as that found in MnFe_2O_4 prepared using conventional solid-state ceramic methods.⁵⁷ Different cation distributions over tetrahedral and octahedral sites in manganese ferrites have been associated with different synthetic methods.⁵⁸ However, the way different synthetic routes affect the cation distribution in the structure is controversial. Some works report a particle size dependence, showing that the inversion parameter increases with decreasing particle sizes;^{59,60} other works report no size dependence, showing different degrees of inversion for systems having the same particle size.⁶¹ Some previous works suggest that the different degree of inversion observed for systems prepared using different conditions can be related to the oxidation state of the cations. It has been shown that different preparation conditions of Mn ferrite can induce partial oxidation of manganese ions which can lead to a different distribution of Mn and Fe cations in the crystalline structure.³⁶ A higher degree of inversion is expected for samples containing Mn^{3+} because Mn^{3+} shows a preference for octahedral sites due to the higher crystal field stabilization energy for octahedral coordination.⁶² In the present case, the thermal treatment of the AFeMn sample performed under argon flow allowed us to avoid the oxidation of Mn^{2+} , as confirmed by XANES.

Bulk CoFe_2O_4 is a *partially inverted* spinel structure reported to have cobalt atoms predominantly in the octahedral sites ($i = 0.68$ – 0.80).^{22–26} In this work, the results of the fitting of the AFeCo sample indicate an inversion parameters of 0.68, in agreement with data reported for bulk CoFe_2O_4 .²⁶

Bulk NiFe_2O_4 has a totally inverted spinel structure where all of the Ni^{2+} ions occupy octahedral sites and the Fe^{3+} ions are equally distributed between tetrahedral and octahedral sites. However, there are reports in the literature which show a different cation distribution between bulk and nanosized ferrites. A mixed spinel structure in which part of the Ni^{2+} ions occupy tetrahedral sites has been suggested for NiFe_2O_4 nanoparticles (10 nm) prepared by high-energy ball-milling on the basis of Mössbauer spectroscopy and qualitative EXAFS analysis.¹¹ In a similar study on slightly smaller NiFe_2O_4 nanoparticles (3–4 nm) prepared by hydrolysis in a polyol medium,⁶³ it was estimated that 10% of the Ni^{2+} ions occupy tetrahedral sites and 90% octahedral sites. However, Nielsen et al. reported that

the inverse structure of bulk NiFe_2O_4 is preserved at the nanometer scale on NiFe_2O_4 nanoparticles (~ 40 nm) synthesized in near-critical and supercritical water.⁶⁴ In this work, the fitting of the EXAFS oscillations of the nanocomposites AFeNi gave a degree of inversion of 1.0, corresponding to that of bulk NiFe_2O_4 . This is in agreement with the result obtained on cobalt and manganese ferrite nanocomposite aerogels, whose degrees of inversion were found to be similar to the values commonly reported in the literature for the corresponding bulk materials.

Another important finding which indicates that X-ray absorption techniques have superior capability in the structural studies of spinels is the difference between the best fitting Fe–O and M–O distances. Both tetrahedral and octahedral Fe–O distances are shorter compared to M–O distances in agreement with the smaller atomic Fe^{3+} radius compared to M^{2+} . While diffraction methods would only provide average M–O distances in octahedral and tetrahedral sites, due to the selectivity of the EXAFS technique, the environment of Fe^{3+} and M^{2+} can be studied independently, so that the individual distances can be determined.

Magnetic Measurements. Zero-field-cooled (ZFC) magnetizations were measured by cooling the AFeMn, AFeCo, and AFeNi samples in a zero magnetic field and then increasing the temperature in a static field of 25 Oe, while field-cooled (FC) curves were obtained by cooling the samples in the same static field. The observed irreversibility is due to the characteristic blocking–unblocking process of the particle magnetic moment when thermal energy is changed. As the relaxation time of a magnetic particle increases with decreasing temperature, we can define, for a certain observation time, a characteristic temperature, called the blocking temperature, below which the particle moment appears blocked with respect to the time scale of the experiment. At the blocking temperature (T_B), the thermal energy $k_B T$ ($T = T_B$ and k_B is the Boltzmann's constant) equals the energy barrier for the magnetic moment reversal associated with the total anisotropy energy, E_B , which as a first approximation is proportional to the particle volume V , $E_B = K_{\text{eff}} V$, where K_{eff} is the anisotropy energy density. At temperatures higher than T_B , the single particle magnetic moment progressively unblocks and the magnetization in the presence of a magnetic field reaches its thermal equilibrium value, mimicking an atomic paramagnet. However, since the magnetic moment of a single particle is much higher than that of an atom, the magnetic state for $T > T_B$ is called superparamagnetic. In this state, the remanence and coercivity of the system vanish.⁶⁵

In the real case of an ensemble of magnetic nanoparticles, with easy axis randomly distributed over the entire space and with a certain size distribution, even the total anisotropy energy barrier is distributed over a certain range. For this reason, since the blocking temperature and anisotropy constant are measured on the entire nanoparticle ensemble, they have to be considered as mean values. The blocking temperature T_B is assumed to be equal to the thermal value corresponding to the maximum of the ZFC curve, as usually reported. The temperature at which the ZFC and FC curves split (T_{cross}) corresponds to the deblocking of magnetic moment of the largest particles. Consequently, the difference between T_B and T_{cross} gives an indication of the narrowness of the anisotropy energy barrier distribution of the particles.

The magnetic properties of the AFeMn, AFeCo, and AFeNi samples are in agreement with those expected for an assembly of randomly oriented single domain particles. The temperature dependence of the zero-field-cooled and field-cooled magnetizations, measured with an applied field of 25 Oe, is shown in

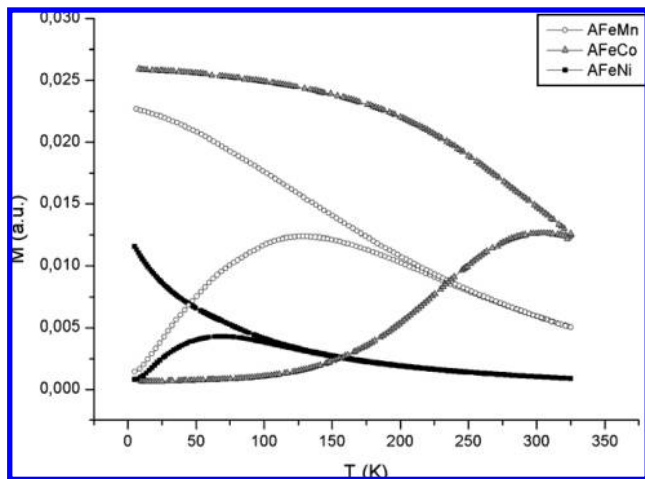


Figure 6. ZFC and FC magnetizations of AFeMn, AFeCo, and AFeNi samples, measured with a magnetic field of $H = 25$ Oe.

Figure 6. The ZFC magnetization clearly exhibits a maximum at 70 K for the sample AFeNi, at 129 K for the sample AFeMn, and at 303 K for the sample AFeCo, indicating that the different ferrite particles are characterized by a different average energy barrier. The T_{cross} value is equal to 230 K for the AFeNi sample and to 285 K for the AFeMn sample, while the value for the AFeCo sample is unknown, being higher than the maximum temperature (325 K) reached in the measurement.

For ZFC/FC measurements, it is usually assumed that⁶⁶

$$K_{\text{eff}}V = 25k_B T_B \quad (3)$$

K_{eff} contains all of the different contributions to the effective anisotropy given by the magnetocrystalline, shape, surface, and stress magnetic anisotropies. Moreover, a further contribution to the effective magnetic anisotropy can be given by the presence of dipolar and/or exchange interactions among the particles.⁶⁷

If one considers the particle mean size d for each sample, as determined by Sherrer analysis, by using eq 3, a first rough determination of K_{eff} is possible. K_{eff} results to be 1.17×10^6 , 9.24×10^6 , and 2.14×10^6 erg/cm³ for AFeMn, AFeCo, and AFeNi samples, respectively. All of these values are much higher than those reported for the manganese cobalt and nickel bulk ferrites (0.025×10^6 ,⁶⁸ 1.8×10^6 ,⁶⁹ and 0.07×10^6 erg/cm³,⁷⁰ respectively), as expected for nanosized particles, where the high surface anisotropy plays a fundamental role in increasing the total anisotropy. From these data, the surface contribution K_S to the total magnetic anisotropy energy density was estimated by assuming $K_{\text{eff}} = K_V + (6/d)K_S$,⁷¹ obtaining 1.73×10^{-1} , 7.44×10^{-1} , and 2.07×10^{-1} erg/cm² for AMnFe, ACoFe, and ANiFe samples, respectively. The values of K_{eff} are reported in Table 4, together with the parameters extracted from the low-temperature hysteresis loops. However, as previously pointed out, a contribution to the total anisotropy rising from interparticle interactions cannot be completely ruled out, due to the relatively high amount of ferrite phase in the samples. In fact, even if the occurrence of exchange interactions (that require contact among the particles to be established) can be excluded due to the nanoparticle dispersion in a highly porous silica host, the presence of dipolar interactions is very likely, which would give rise to a non-negligible contribution to the total anisotropy. Such kinds of interactions are well-known to increase with the volume of the particles (i.e., with the particle magnetic moment) and to decrease with the mean distance among them.⁷² In the case of the sample AFeCo and similar

TABLE 4: Parameters Obtained from the ZFC/FC Static Magnetizations Measurements (Reported in Figure 6) and from the Low-Temperature Hysteresis Loops (Reported in Figure 7)^a

sample	T_B (K)	T_{cross} (K)	K_{eff} (erg/cm ³)	H_C (Oe)	M_S (emu/g)	ferrite wt %	M_r/M_S
AFeMn	129	285	1.17×10^6	316	11.2	10.1	0.12
AFeCo	303	>325	9.24×10^6	14286	9.9	10.6	0.46
AFeNi	70	230	2.14×10^6	542	5.6	10.0	0.13

^a T_B (K), blocking temperature; T_{cross} (K), temperature at which ZFC and FC magnetization superimpose; K_{eff} (erg/cm³), effective anisotropy constant; H_C (Oe), coercive field; M_S (emu/g), extrapolated saturation magnetization; ferrite wt %, wt % ferrite content as determined by comparison with $M_{S,\text{bulk}}$ of the corresponding bulk ferrite (from the literature); M_r/M_S , remnant reduced magnetization.

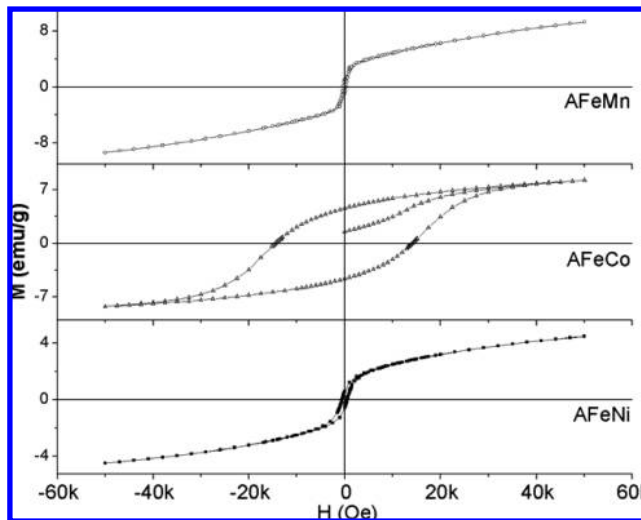


Figure 7. Hysteresis loop of AFeMn, AFeCo and AFeNi samples, collected at $T = 5$ K.

systems, the role of interactions was extensively studied in our previous work.⁷³

Figure 7 shows the isothermal hysteresis loops collected at $T = 5$ K for the three samples. Table 4 summarizes the parameters obtained from these measurements. The hysteresis curves of the AFeMn and AFeNi samples do not reach complete saturation even at 50 kOe. This is often observed in nanosized materials and can be ascribed to the presence of a spin disordered surface layer which requires a larger field to be saturated together with the concomitant effect of the small mean size of nanoparticles with not too high anisotropy: a non-negligible fraction of them are still fast relaxing even at 50 kOe. On the contrary, the case of the AFeCo sample is quite different, due to the much larger magnetocrystalline anisotropy characteristic of the cobalt ferrite; in this case, all of the particles are already almost completely oriented for a field of around 40 kOe. The low M_r/M_S value obtained for AFeMn and AFeNi may indicate that a significant amount of nanoparticles are still superparamagnetically fast relaxing at 5 K, when the external magnetic field is turned off. However, also the presence of a frustrated surface spin layer, as suggested by the lack of saturation of the magnetization curve, can strongly contribute to the decrease of the remnant magnetization. On the contrary, the M_r/M_S value of 0.46 found for the AFeCo sample is almost equal to 0.5, the value expected for randomly oriented and completely blocked nanoparticles.

The coercive fields measured for the three samples are all much higher than those reported in the literature for each ferrite

in its bulk form, as expected for nanosized particles. Their values are in agreement with the trend measured for the anisotropy constant.

The saturation magnetization (M_s) was determined from a plot of M versus $1/H$, extrapolating the M values for $1/H \rightarrow 0$.⁷⁴ The small diamagnetic contribution due to the silica matrix was always neglected. Moreover, the wt % of ferrite contained in each sample was estimated by comparison with the saturation magnetization value ($M_{s,\text{bulk}}$) reported in the literature for the corresponding bulk ferrite. $M_{s,\text{bulk}}$ is equal to 110 emu/g for bulk MnFe_2O_4 ,⁷⁵ 93.9 emu/g for bulk CoFe_2O_4 ,⁷⁶ and 56 emu/g for bulk NiFe_2O_4 .⁷⁷ The corresponding ferrite wt % of each sample, which is also reported in Table 4, is very close to the expected value of 10% for all samples. Several studies (see, for instance, refs 78–81) clearly report that a change in the degree of inversion can dramatically affect all of the magnetic features (magnetization, coercive field, Curie temperature) of different types of ferrite; thus, in principle, the latter can be used to infer information on the inversion degree. However, as discussed above, in this case, these magnetic parameters cannot be taken into account, since they are affected by the nanometric size of the materials. However, as we found low-temperature saturation magnetization values very close to the bulk ones and as they are expected to be extremely dependent on the inversion degree, they can be assumed as a reasonable confirmation of the results obtained by the XAS studies: the degree of inversion of the nanoparticles of nickel, manganese, and cobalt ferrite in the three samples is very similar to the values reported in the literature for the corresponding bulk ferrites.

4. Conclusions

Nanoparticles of Mn, Co, and Ni ferrites with average crystal sizes between 6 and 9 nm dispersed in a highly porous aerogel silica matrix were prepared, which result to have the spinel structure with an increasing degree of inversion. X-ray absorption spectroscopy was confirmed to be an extremely powerful technique to study the cation distribution in spinel ferrites due to the possibility to study independently and separately the oxidation state and the structural environment of Fe on one side and either Mn, Co, or Ni on the other side. In fact, the EXAFS FTs vary considerably in the region 2.5–4 Å depending on the distribution of the cations between the octahedral and tetrahedral sites of the spinel structure. As a consequence, a qualitative comparison of the FTs in the region 2.5–4 Å provides a rough estimate of the Fe^{3+} and M^{2+} distribution between the octahedral and tetrahedral sites of the spinel structure and therefore of the degree of inversion. Moreover, quantitative information on the degree of inversion can be obtained by fitting the EXAFS data with separate parameters for the cations in octahedral and tetrahedral sites. This approach indicates that the degree of inversion is increasing from 0.20 for Mn ferrite nanoparticles to 0.68 for Co ferrite nanoparticles and to 1.00 for Ni ferrite nanoparticles. All of these values are very similar to what is commonly found in the corresponding bulk ferrites, suggesting that particle size does not influence significantly the degree of inversion. The magnetic characterization is in agreement with these findings.

Acknowledgment. The authors wish to thank Elettra XAFS beamline scientists Luca Olivi and Andrea Cognigni and SRS Station 7.1 beamline scientist Steven G. Fiddy for assistance during data collection. Beamtime at Daresbury Laboratory was supported by the European Community-Access of Research Infrastructure action of the Improving Human Potential Pro-

gramme. This work was supported by a European Community Sixth Framework Programme Marie Curie Intra-European Fellowship (Contract MEIF-CT-2005-024995) and by Royal Society Award (Grant 27221340).

Supporting Information Available: XANES spectra of Mn, Co, Ni, and Fe reference compounds. This material is available free of charge via the Internet at <http://pubs.acs.org>.

References and Notes

- (1) Verwey, J. W.; Heilmann, E. L. *J. Chem. Phys.* **1947**, *15*, 4.
- (2) Sickafus, K. E.; Wills, J. M. *J. Am. Ceram. Soc.* **1999**, *82*, 12.
- (3) Harris, V. G.; Koon, N. C.; Williams, C. M.; Zhang, Q.; Abe, M.; Kirkland, J. P. *Appl. Phys. Lett.* **1996**, *68*, 15.
- (4) Mathew, D. S.; Juang, R.-S. *Chem. Eng. J.* **2007**, *129*, 51.
- (5) Han, D. H.; Luo, H. L.; Yang, Z. *J. Magn. Magn. Mater.* **1996**, *161*, 376.
- (6) Tae-Jong, Y.; Jun Sung, K.; Byung Geol, K.; Kyeong Nam, Y.; Myung-Haing, C.; Jin-Kyu, L. *Angew. Chem., Int. Ed.* **2005**, *44*, 1068.
- (7) Cunningham, C. H.; Arai, T.; Yang, P. C.; McConnell, M. V.; Pauly, J. M.; Connolly, S. M. *Magn. Reson. Med.* **2005**, *53*, 999.
- (8) Giri, A. K.; Pellerin, K.; Pongsaksawad, W.; Sorescu, M.; Majetich, S. A. *IEEE Trans. Magn.* **2000**, *36*, 3029.
- (9) Tang, Z. X.; Sorensen, C. M.; Klabunde, K. J.; Hadjipanyis, G. C. *Phys. Rev. Lett.* **1991**, *67*, 3602.
- (10) Cote, L. J.; Teja, A. S.; Wilkinson, A. P.; Zhang, Z. *J. Fluid Phase Equilib.* **2003**, *210*, 307.
- (11) Chinnasamy, C. N.; Narayanasamy, A.; Ponpandian, N.; Chattopadhyay, K.; Shinoda, K.; Jeyadevan, B.; Tohji, K.; Nakatsuka, K.; Furubayashi, T.; Nakatani, I. *Phys. Rev. B* **2001**, *63*, 184108.
- (12) Morrison, A. H.; Haneda, K. *J. Appl. Phys.* **1981**, *52*, 2496.
- (13) Ramalho, M. A. F.; Gama, L.; Antonio, S. G.; Paiva-Santos, C. O.; Miola, E. J.; Kiminami, R. H. G. A.; Costa, A. C. F. M. *J. Mater. Sci.* **2007**, *42*, 3603.
- (14) Misra, R. K. D.; Gubbala, S.; Kale, A.; Egelhoff, W. F., Jr. *Mater. Sci. Eng., B* **2004**, *111*, 164.
- (15) Li, L.; Li, G.; Smith, R. L., Jr.; Inomata, H. *Chem. Mater.* **2000**, *12*, 3705.
- (16) Silva, J. B.; Diniz, C. F.; Lago, R. M.; Mohallem, N. D. S. *J. Non-Cryst. Solids* **2004**, *348*, 201.
- (17) Zhang, S.; Dong, D.; Sui, Y.; Liu, Z.; Wang, H.; Qian, Z.; Su, W. *J. Alloys Compd.* **2006**, *415*, 257.
- (18) Huang, X.-H.; Chen, Z.-H. *Solid State Commun.* **1999**, *111*, 287.
- (19) Zuo, X.; Yang, A.; Yoon, S.; Christodoulides, J. A.; Harris, V. G.; Vittoria, C. *J. Appl. Phys.* **2005**, *97*, 10G103.
- (20) Wang, J.; Wu, Y.; Zhu, Y. *Int. J. Mod. Phys. B* **2007**, *21*, 723.
- (21) Kravtsov, E.; Haskel, D.; Cady, A.; Yang, A.; Vittoria, C.; Zuo, X.; Harris, V. G. *Phys. Rev. B* **2006**, *74*, 104114.
- (22) Vaingankar, A. S.; Khasbardar, B. V.; Patil, R. N. *J. Phys. F: Met. Phys.* **1980**, *10*, 1615.
- (23) Inoue, T. *J. Electrochem. Soc. Jpn.* **1955**, *23*, 24.
- (24) Vaingankar, A. S.; Patil, S. A.; Sahasrabudhe, V. S. *Trans. Indian Inst. Met.* **1981**, *34*, 5.
- (25) Prasad, R.; Moorthy, V. K. *Trans. Indian Ceram. Soc.* **1970**, *29*, 4.
- (26) Carta, D.; Mountjoy, G.; Navarra, G.; Casula, M. F.; Loche, D.; Marras, S.; Corrias, A. *J. Phys. Chem. C* **2007**, *111*, 6308.
- (27) Hastings, J. M.; Corliss, L. M. *Rev. Mod. Phys.* **1953**, *25*, 114.
- (28) Moscovici, J.; Michalowicz, A.; Decker, S.; Lagadic, I.; Latreche, K.; Klabunde, K. *J. Synchrotron Radiat.* **1999**, *6*, 604.
- (29) Moscovici, J.; Benzakour, M.; Decker, S.; Carnes, C.; Klabunde, K.; Michalowicz, A. *J. Synchrotron Radiat.* **2001**, *8*, 925.
- (30) Carta, D.; Corrias, A.; Mountjoy, G.; Navarra, G. *J. Non-Cryst. Solids* **2007**, *353*, 1785.
- (31) Corrias, A.; Mountjoy, G.; Piccaluga, G.; Solinas, S. *J. Phys. Chem. B* **1999**, *103*, 10081.
- (32) Carta, D.; Mountjoy, G.; Gass, M.; Navarra, G.; Casula, M. F.; Corrias, A. *J. Chem. Phys.* **2007**, *127*, 204705.
- (33) Koningsberger, D. C.; Prins, R. *X-ray Absorption. Principles, Applications, Techniques of EXAFS, SEXAFS and XANES*; Wiley: New York, 1988.
- (34) Carta, D.; Casula, M. F.; Mountjoy, G.; Corrias, A. *Phys. Chem. Chem. Phys.* **2008**, *10*, 3108.
- (35) Carta, D.; Loche, D.; Mountjoy, G.; Navarra, G.; Corrias, A. *J. Phys. Chem. C* **2008**, *112*, 15623.
- (36) Zhang, J.; Wang, Z. L.; Chakoumakos, C.; Yin, J. S. *J. Am. Chem. Soc.* **1998**, *120*, 1800.
- (37) Lee, J.-G.; Park, J. Y.; Kim, C. S. *J. Mater. Sci.* **1998**, *33*, 3965.
- (38) Klug, H. P.; Alexander, L. E. *X-ray Diffraction Procedures*; Wiley: New York, 1974.

- (39) Klementiev, K. V. *Appl. Phys.* **2001**, *34*, 209.
- (40) Tomic, S.; Searle, B.G.; Wander, A.; Harrison, N. M.; Dent, A. J.; Mosselmans, J. F. W.; Inglesfield, J. E. *CCLRC Technical Report DL-TR-2005-001*, ISSN 1362-0207, CCRLC, Warrington, UK, 2004.
- (41) Gurman, S. J.; Binsted, N.; Ross, I. *J. Phys. C* **1984**, *17*, 143.
- (42) Von Barth, U.; Hedin, L. *J. Phys. C* **1972**, *5*, 1629.
- (43) Crozier, E. D. *Nucl. Instrum. Methods Phys. Res., Sect. B* **1997**, *133*, 134.
- (44) Error Report of the International XAFS Society Standards and Criteria Committee (http://ixs.iit.edu/subcommittee_reports/sc/), 2000.
- (45) Bianconi, A. In *X-ray absorption: principles, applications, techniques of EXAFS, SEXAFS and XANES*; Koningsberger, D. C., Prins, R., Eds.; Wiley: New York, 1988; Chapter 11.
- (46) Grunes, L. A. *Phys. Rev. B* **1983**, *27*, 2111.
- (47) Wilke, M.; Farges, F.; Petit, P.-E.; Brown, G. E.; Martin, F. *Am. Mineral.* **2001**, *86*, 714.
- (48) Westre, T. E.; Kennepohl, P.; DeWitt, J. G.; Hedman, B.; Hodgson, K. O.; Solomon, E. I. *J. Am. Chem. Soc.* **1997**, *119*, 6297.
- (49) Farges, F.; Brown, G. E.; Petit, P.-E.; Munoz, M. *Geochim. Cosmochim. Acta* **2001**, *65*, 1665.
- (50) Waychunas, G. A.; Apter, M. J.; Brown, G. E. *Phys. Chem. Mater.* **1983**, *10*, 1.
- (51) Farges, F. *Phys. Rev. B* **2005**, *71*, 155109.
- (52) Corrias, A.; Navarra, G.; Casula, M. F.; Marras, S.; Mountjoy, G. *J. Phys. Chem. B* **2005**, *109*, 13964.
- (53) PDF card 10-391.
- (54) PDF card 22-1086.
- (55) PDF card 10-325.
- (56) Greigor, R. B.; Lytle, F. W. *J. Catal.* **1980**, *63*, 476.
- (57) Harrison, F. W.; Osmond, W. P.; Teale, R. W. *Phys. Rev.* **1957**, *105*, 5.
- (58) Ferreira, T. A. S.; Waerenborgh, J. C.; Mendonça, M. H. R. M.; Nunes, M. R.; Costa, F. M. *Solid State Sci.* **2003**, *5*, 383.
- (59) Van der Zaag, P. J.; Brabers, V. A. M.; Johnson, M. T.; Noordermeer, A.; Bongers, P. F. *Phys. Rev. B* **1995**, *51*, 17.
- (60) Mahmoud, M. H.; Hamdeh, H. H.; Abdel-Mageed, A. I.; Abdallah, A. M.; Fayek, M. K. *Physica B* **2000**, *291*, 49.
- (61) Kulkarni, G. U.; Kanna, K. R.; Arunarkavalli, T.; Rao, C. N. R. *Phys. Rev. B* **1994**, *49*, 724.
- (62) Chen, J. P.; Sorensen, C. M.; Klabunde, K. J.; Hadjipanayis, G. C.; Devlin, E.; Kostikas, A. *Phys. Rev. B* **1996**, *54*, 13.
- (63) Chkoundali, S.; Ammar, S.; Jouini, N.; Fiévet, F.; Molinié, P.; Danot, M.; Villain, F.; Grenèche, J.-M. *J. Phys.: Condens. Matter* **2004**, *16*, 4357.
- (64) Nilsen, M. H.; Nordhei, C.; Ramstad, A. L.; Nicholson, D. G.; Poliakoff, M.; Cabañas, A. *J. Phys. Chem. C* **2007**, *111*, 6252.
- (65) Néel, L. *Ann. Geophys.* **1949**, *5*, 99.
- (66) Kneller, E. F.; Luborsky, F. E. *J. Appl. Phys.* **1963**, *34*, 656.
- (67) Garcia-Otero, J.; Porto, M.; Rivas, J.; Bunde, A. *Phys. Rev. Lett.* **2000**, *84*, 63.
- (68) Vestal, C. R.; Song, Q.; Zhang, Z. J. *J. Phys. Chem. B* **2004**, *108*, 18222.
- (69) Buschow, K. H. J. *Handbook of Magnetic Materials*; North-Holland: Amsterdam, The Netherlands, 1995; Vol. 8, p 212.
- (70) Skomski, R. *J. Phys.: Condens. Matter* **2003**, *15*, r841.
- (71) Bødker, F.; Mørup, S.; Linderöth, S. *Phys. Rev. Lett.* **1994**, *72*, 282.
- (72) El-Hilo, M.; O'Grady, K.; Chantrell, R. W. *J. Magn. Magn. Mater.* **1992**, *114*, 295.
- (73) Casu, A.; Casula, M. F.; Corrias, A.; Falqui, A.; Loche, D.; Marras, S. *J. Phys. Chem. C* **2007**, *111*, 916.
- (74) Ahmed, S. R.; Ogale, S. B.; Papaefthymiou, G. C.; Ramesh, R.; Kofinas, P. *Appl. Phys. Lett.* **2002**, *80*, 1616.
- (75) Balaji, G.; Gajbhiye, N. S.; Wilde, G.; Weißmüller, J. *J. Magn. Magn. Mater.* **2002**, *242–245*, 617.
- (76) Lee, E. W.; Bishop, J. E. L. *Proc. Phys. Soc.* **1966**, *89*, 661.
- (77) Sepelak, V.; Tkacova, K.; Boldyrev, V. V.; Wibmann, S.; Becker, K. D. *Physica B* **1997**, *617*, 234.
- (78) Tung, L. D.; Kolesnichenko, V.; Caruntu, D.; Chou, N. H.; O'Connor, C. J.; Spinu, L. *J. Appl. Phys.* **2003**, *93*, 1486.
- (79) Zuo, X.; Yang, A.; Yoon, S.-D.; Christodoulides, J. A.; Harris, V. G.; Vittoria, C. *J. Appl. Phys.* **1997**, *10G103*, 1.
- (80) Sepelak, V.; Baabe, D.; Becker, K. D. *J. Mater. Syn. Proc.* **2000**, *8*, 333.
- (81) Simsa, Z.; Brabers, V. *IEEE Trans. Magn.* **1975**, *11*, 1303.